Copper(I) and Copper(II) Coordination Structure under Hydrothermal Conditions at 325 °C: An X-ray Absorption Fine Structure and Molecular Dynamics Study

John L. Fulton,* Markus M. Hoffmann, John G. Darab, and Bruce J. Palmer*

Environmental and Health Sciences Division, Pacific Northwest National Laboratory,† Richland, Washington 99352

Edward A. Stern*

Physics Department, University of Washington, Seattle, Washington 98195

Received: May 26, 2000; In Final Form: September 13, 2000

X-ray absorption fine structure (XAFS) spectroscopy was used to measure the coordination structure about Cu^{2+}, Cu^{1+}, and Br^- in water at temperatures up to 325 °C. The hexaaqua Cu^{2+} species maintains its distorted octahedral structure up to 325 °C, whereas at higher temperatures, dehydration reactions occur producing CuO. Under reducing conditions, the dibromo Cu^{1+} species, $[CuBr_2]^-$, is predominant at 200 °C and above for systems having excess Br^-. Even for a very high salt concentration of 2.0 *m* NaBr, only the dibromo Cu^{1+} species, $[CuBr_2]^-$, is observed with no evidence of higher Br^- coordination. For this dibromo-species there are no tightly bound hydration waters in the first shell. In the absence of excess Br^-, a monoaqua monobromo Cu^{1+} species, $[Cu(H_2O)Br]$ is observed. For certain systems, both Cu *and* Br XAFS were acquired, and a global model was used to fit the two independent sets of XAFS data. Thus, the results represent a complete picture of the coordination structure about Cu^{1+} including the coordination numbers, distances for the ion−ion and water-ion associations and also a high-quality measurement of the binding strength and amount of disorder (Debye−Waller factor and the anharmonicity) of the Cu^{1+}/Br^- association. Molecular dynamics (MD) simulations were used to further explore the structure and the binding forces for the $[CuBr_2]^-$ species under hydrothermal conditions. We found quantitative agreement for the Cu−Br interactions, but the simulation has difficulty predicting the experimental Cu−H_2O interaction. In particular, the amount of scattering from the water in the dibromo Cu^{1+} complex was highly over-predicted, so that it is clear that simple intermolecular potential models do not adequately capture this structural feature.

Introduction

X-ray absorption fine structure (XAFS) studies of ions in water at high temperatures are providing important insights on the exact nature of ion−water and ion−ion associations.[1−9] These results are improving our understanding of geochemical processes, power plant corrosion, and waste destruction under hydrothermal conditions. In general, ionic species that would be fully dissociated from their respective counterions and completely hydrated with water under ambient conditions, start to associate with the counterion at elevated temperatures. This behavior is strongly enhanced above about 300 °C where the hydrogen bond structure of water becomes too weak to sufficiently screen the charges of dissolved ions and, thus, the electrostatic interactions between oppositely charge species draw them together into contact ion pairs. Clearly, describing the structure of the first coordination shell is of utmost importance for understanding the underlying thermodynamics of these systems. XAFS studies are perfectly suited to yield this information about the first-shell structure around ions and numerous studies have now demonstrated that this technique is suitable to temperatures well above 400 °C for these aqueous systems.[1,7]

XAFS studies of hydrothermal systems are also providing new insights into the behavior of ions that are relevant to a vast array of *ambient* processes. Under ambient conditions, there are only a few ion−ion coordination species and there generally exists only one type of hydration species. Model development thus is limited to a myopic view of the coordination structure. In contrast, at high temperatures the electrostatic interactions are activated and a wide range of ion−ion associations can be studied. There is already much evidence that existing ion−ion molecular potentials that have been formulated from ambient data do not adequately capture the true structure of ion pair species.[4,7] First attempts at improving these models have been initiated and the eventual result will be models of ion behavior that will realistically represent the behavior under hydrothermal *and* ambient conditions.

In this report, we explore the behavior of the transition metal copper under ambient and hydrothermal conditions in differing redox environments. A better knowledge of the redox chemistry in aqueous solutions containing Cu^{1+} and Cu^{2+} will, for example, improve our fundamental understanding of geochemical systems and corrosion phenomena in power plants. Under hydrothermal conditions, Cu^{1+} species are often thermodynamically favored. $[CuCl_2]^-$ is an important species for transport of copper in geochemical systems.[10,11] In this study, we have chosen the chemically similar Br^- as the counterion since it is well suited for characterization by XAFS. For Br, the favorable

* To whom correspondence should be addressed: E-mail: john.fulton@pnl.gov, bruce.palmer@pnl.gov, and stern@phys.washington.edu. Fax: 509-376-0418.

† Operated by Battelle Memorial Institute.

10.1021/jp001949a CCC: $19.00
Published on Web 11/11/2000

backscattering amplitudes and phase shifts provide an ideal system for the quantitative characterization of the halocuprate-(I) complexes.

Under ambient conditions the hexaaqua Cu^{2+} ion is the predominant soluble species at low to moderate concentrations. It is well-known that a Jahn−Teller distortion of the octahedral site occurs. This typically leads to a tetragonal structure with four short, equivalent $Cu-H_2O$ bonds and two longer axial bonds. Detailed XAFS and neutron diffraction studies of this species have recently been reported,[12−14] and there is a recent study of Cl^- complexation to Cu^{2+} at temperatures up to 175 °C.[15] The low solubility of Cu^{1+} in ambient water makes studies of its structure more difficult. However, $[CuBr_2]^-$ is soluble in polar organic liquids such as acetonitrile and dimethyl sulfoxide. The linear $[CuBr_2]^-$ species under ambient conditions is reported to have a Cu−Br bond distance of 2.21 Å in acetonitrile and 2.24 Å in dimethyl sulfoxide.[16] What is also an interesting observation from the same study is that the linear dihalo Cu^{1+} species exhibits *no* coordination of the aprotic solvent directly to Cu^{1+} even though the direct interaction of this ion with the solvent should not be sterically hindered.

We report the first-shell structure of water about Cu^{2+} at temperatures up to 325 °C. We also investigate the coordination of Cu^{1+} by Br^- under that same conditions. A great deal of information about the chemical environment of copper can be derived from XAFS. Oxidation state and the coordination structure can be determined from the X-ray absorption preedge peak and the X-ray absorption near-edge structure (XANES). In this report, this information is first used to quantify the redox changes that occur in the Cu system. Subsequent measurement of the extended X-ray absorption fine structure (EXAFS) in the region up to about 700 eV above the edge is used to determine the coordination structure. To greatly improve our confidence in the structure of the Cu−Br ion pair species, we conducted separate EXAFS measurements on *both* the cation (Cu *K*-edge) and the anion (Br *K*-edge) for certain solutions under identical conditions. A global fit of these two data sets provides high confidence in the measured parameters. Finally, we use molecular dynamics (MD) simulation to validate the methods of EXAFS analysis and then to test the performance of the various intermolecular potentials under high-temperature conditions.

Experimental and Simulation Methods

Experimental Methods. XAFS spectra were acquired using two high-pressure cells of slightly different design. Both cells used synthetic single-crystal diamond X-ray windows that were mounted in such a way as to provide a 2.0 mm path length inside the cell. One cell used a flow cell approach in which various aqueous solutions could be introduced directly into the cell using a high-pressure syringe pump. This cell has been described in detail previously.[17,18] The other cell was of a static or "batch" design such that solutions were prepared and loaded under ambient conditions and then sealed between the two X-ray windows. For the flow cell design, the materials of the internal wetted-surfaces (cell and transfer lines) are constructed from only two materials: a special corrosion resistant Pt/10%Ir alloy and the diamond X-ray windows. This combination of materials normally provides high corrosion resistance to a wide variety of aqueous solutions. In all cases, the starting solution either contained $CuBr_2$ or $Cu(NO_3)_2$ with varying amounts of added salts or acids. At elevated temperatures the Cu(II) compounds can undergo a reduction to Cu(I). In the course of these studies, it was discovered that the copper(II) bromide solutions containing excess NaBr at high temperature will readily oxidize Pt^0 to a new bromo-platinum(II) species. Thus, to eliminate possible conflicting contributions from dissolved Pt species the copper-(II) bromide solutions were also run in the microreactor batch cell. For the batch cell, the *only* wetted materials are Cu^0 and the diamond windows. As described below, the high-temperature Cu XAFS of the dissolved $Cu^{1+}Br_n$ were found to be identical in both cells and hence interference from dissolved Pt species did not affect the Cu coordination. We also found, that during the acquisition of a high-temperature spectrum the Cu speciation does not change with time. For many of the reported high-temperature conditions a replicate spectrum was acquired that, in all cases, was found to be identical to the initial spectrum.

The cells were clad in multiple layers of a fiber insulating material and then placed in a vacuum can in order to minimize both the radiative and convective heat losses. This method provides a high-degree of temperature uniformity that is essential for obtaining the lowest noise XAFS spectra. The temperature of the cell was maintained to within ±1 °C using a three-mode controller (Omega, No. CN3000) with platinum resistive probes, and the fluid pressure was measured for the flow-cell studies within ±1 bar using an electronic transducer (Precise Sensors, Inc., No. D451). The single-crystal diamond XAFS windows were used to acquire both the Cu and the Br XAFS. In obtaining the copper *K*-edge (8979 eV) data, the windows have no contribution to the background function. However, at the higher-energy Br *K*-edge (13474 eV), the single-crystal diamond windows produce a series of Bragg reflections that must be manually removed from the spectra. In previous studies,[17,18] the much weaker and highly diffuse Bragg contributions from polycrystalline diamond windows (higher energy range) were effectively removed by subtracting a background spectra of pure water taken under identical conditions of the sample spectra. However, for the static cell this method is not practical and thus manual removal of 3−4 Bragg peaks is required. By making slight adjustments to the angle of the cell with respect to the beam, the number of Bragg peaks can be minimized and their location can be shifted away from the critical region of the EXAFS spectrum. For the two reported Br EXAFS spectra, there were about 3 or 4, very narrow-bandwidth Bragg peaks that were removed by deleting the two or three affected data points in the spectra. Although this simple procedure for removal of Bragg peaks is successful, as shown in the Br XAFS spectra of Figures 9 and 11, there are other cases where difficulties are encountered in using these types of procedures.[19]

Copper *K*-edge (8979 eV) XAFS spectra were collected on the insertion device beamline (PNC−CAT) at the Advanced Photon Source (Argonne National Laboratory). A single scan was sufficient to obtain high quality spectra at APS. The optical setup and tuning was identical to that previously reported.[4] Energy calibration was accomplished using the first inflection point of a Cu foil spectrum. By placing a Cu foil and a third ionization detector immediately downstream from the sample cell ionization detector, the stability of the calibrated monochromator energy was checked for all spectra by simultaneously acquiring a Cu foil spectrum. The solution densities, or in certain instances the Cu concentrations, were accurately determined from the height of the copper absorption edge.[3] Anhydrous $CuBr_2$ with a reported purity of 98% was used as received from Alfa Aesar. All solutions were de-oxygenated by purging with N_2 prior to use. To reduce the likelihood of copper hydrolysis reactions at 325 °C the starting solutions were acidified with either HBr or HNO_3 to a starting pH of 1.5 prior to heating.

Analysis of the EXAFS data[20−22] was accomplished using well-established methods that are part of the UWXAFS program.[23] The standard EXAFS relationship is given by

$$\chi(k) = \sum_i \frac{F_i(k) S_0^2 N_i}{kR_i^2} e^{-2k^2\sigma_i^2} e^{-2R_i/\lambda(k)} \times \sin\left(2kR_i + \delta_i(k) - \frac{4}{3}k^3 C_{3,i}\right) \quad (1)$$

The EXAFS oscillations, $\chi(k)$, were extracted from the experimentally measured absorption coefficient using an automated background subtraction method (AUTOBK) developed by Newville et al.[24] The wavenumber of the ejected photoelectron is given by $k = \sqrt{2m_e(E-E_0)/\hbar^2}$ with E_0 being the absorption edge energy. In eq 1, $F_i(k)$, $\delta_i(k)$, and $\lambda(k)$ are the amplitude, phase and mean-free path factor, respectively, that are derived from the theoretical standards calculated by FEFF.[25] The sum in eq 1 is over all possible single scattering paths and for all the significant multiple scattering paths that are calculated to describe the effective scattering amplitudes and phases. We used a core-hole factor of $S_0^2 = 0.85$ for Cu that was measured by others for copper metal foil.[26] We evaluated this S_0^2 value on four solid standards including Cu(II)O, Cu_2(I)O, Cu(II)Br_2, and Cu(I)Br, and found that it was accurate to within approximately 20% for these other copper compounds. The fitted parameters in eq 1 include N_i, the coordination number of the shell for each type of neighboring atom, R_i, the shell distance, σ_i^2, the Debye−Waller factor, which represents the mean-square variation in R_i due to both static and thermal disorder, and finally $C_{3,i}$, the anharmonicity of the pair-distribution. The fitting of the FEFF theoretical standards to the experimental data was accomplished using an analysis program (FEFFIT)[23,27] that employs a nonlinear, least-squares technique. In addition to the structural parameters, a single nonstructural parameter, ΔE_0, is varied to correct for the simple estimate of E_0 made by FEFF.

The Cu $\chi(k)$ data were weighted by k^2, windowed between $1.5 < k < 13.0$ Å^{-1} using a Hanning window with $dk = 1.0$ Å^{-1}. The fits were done on both the real and imaginary parts of $\bar{\chi}(R)$ in the region of $1.5 < R < 5.0$ Å. For Br^{-1}, the detailed procedures for removing the multielectron excitations and the treatment of the amplitude function at low k-values have previously been described.[17] The Br $\chi(k)$ data were weighted by k^2, windowed between $1.75 < k < 8.5$ Å^{-1} using a Hanning window with $dk = 1.0$. The uncertainties reported below (Tables 2−4) are derived from the error analysis routine within the UWAXFS program. The uncertainties correspond to an increase in the misfit (defined by a scaled sum of squares, χ^2_{FEFFIT}) between the data and the best fit model by an amount of $1/\upsilon$, where υ is the degrees of freedom in the fit. For one of the measurements at 325 °C, both Cu and Br EXAFS were acquired on the same system. In this case, a global model was used to *simultaneously* fit both data sets. For this case, the following single scattering paths were included: Cu−Br, Br−O, and Br−Cu. For the Cu−Br and Br−Cu paths, the three parameters, R, σ^2, and C_3, are identical. Also for the Cu−Br and Br−Cu paths, the first shell Br and Cu coordination numbers were constrained by the simple stoichiometric equation, $N_{Cu} = N_{Br}([Cu^{1+}]/[Br^-])$. This relationship defines the number of Br^- anions about a Cu^{1+} cation, N_{Br}, and the number of Cu^{1+} cations about a Br^- anion, N_{Cu}, for *all* soluble Cu^{1+} and Br^- in the system. As an example, for a system containing only $CuBr_2$, if the Cu XAFS measures an average of 1 Br^- about the Cu^{1+}, then the corresponding Br XAFS measurement on the same system would detect an average of 0.5 Cu^{1+} about the Br^- since the remaining free Br^- would be associating only with water and/or Na^+.

TABLE 1: Pair-potential Parameters for the MD Simulations

atom	σ, Å	ϵ, (kcal/mol)	q ($\|e\|$)
O	3.169	0.1553	−0.8476
H	0.000	0.0000	0.4238
Cu	1.550	0.10000	1.0000
Br[a]	4.686	0.1000	−1.0000
Na	2.584	0.1000	1.0000

[a] The Cu−Br value of σ_{ij} was optimized to 2.85 Å to match the experimental result under hydrothermal conditions.

Simulation Methods. The method used to generate EXAFS spectra directly from molecular dynamics simulations has been previously described.[2,4,7,17] These "MD-XAFS" spectra can then be compared to the experimentally derived EXAFS spectra. The method involves first generating a series of molecular configurations from the simulation and then using these configurations as input to the theoretical standard FEFF to generate the EXAFS spectra (MD-XAFS). The simulations of the copper bromide/sodium bromide system at 325 °C were performed using the SPC/E model for water.[28] Parameters for copper were developed as part of this study and parameters for bromide and sodium ion were obtained from Dang.[29,30] The SPC/E model has been successfully used in previous studies of ions in hydrothermal systems.[4,7] The long-range Coulomb interactions were handled using an Ewald summation. The Lennard−Jones and Coulomb parameters σ_i, ϵ_i, and q_i are defined for each atomic species i in Table 1. The Lennard−Jones parameters between different sites were obtained using the standard mixing rules, $\epsilon_{ij} = \sqrt{\epsilon_i \epsilon_j}$ and $\sigma_{ij} = (\sigma_i + \sigma_j)/2$. All parameters used in these calculations are summarized in Table 1. The one exception to using the mixing rules was for the Cu−Br interaction. The parameter σ_{ij} was changed from the mixing rule value of 3.118 Å to 2.850 Å in order to obtain better agreement between the atom distances derived from the experimental and simulated EXAFS spectra. This adjustment is similar to that required for Ni−Br interactions that was made in earlier studies[4] after initial simulations showed large discrepancies between the simulated and experimental Ni−Br distances.

All simulations consisted of 278 rigid water molecules plus one Cu^{1+}, three Na^+ and four Br^-, approximately corresponding to a solution containing 0.20 molal CuBr and 0.4 molal NaBr. The system sizes were adjusted so that the density of the 325 °C solution was 0.69 g/cm^3. Each trajectory was run for a total of 125 ps using a 2.5 fs time step. Every 0.2 ps, a configuration from the simulation was saved to a file, resulting in a total of 625 configurations for each simulation. The cluster about the Cu^{1+} atom was extracted from each configuration. Each cluster contained the central Cu^{1+} atom plus all other atoms, except hydrogen, falling within a cutoff distance, R_c, of the central atom. For Cu^{1+}, the cutoff distance was set at 5 Å. These clusters were used as input for a calculation of the Cu EXAFS spectrum using the FEFF6 multiple-scattering code. The 625 individual Cu spectra were then separately averaged together to obtain a solvent averaged Cu EXAFS spectrum that could be compared directly to the spectrum obtained from the EXAFS experiments.[2]

Experimental Results and Discussion

Chemistry of Cu(I) and Cu(II) Compounds. Three different copper chemistry schemes were examined in this study. The approximate structure for the three main Cu(I,II) species of most interest in this investigation are illustrated in Figure 1.

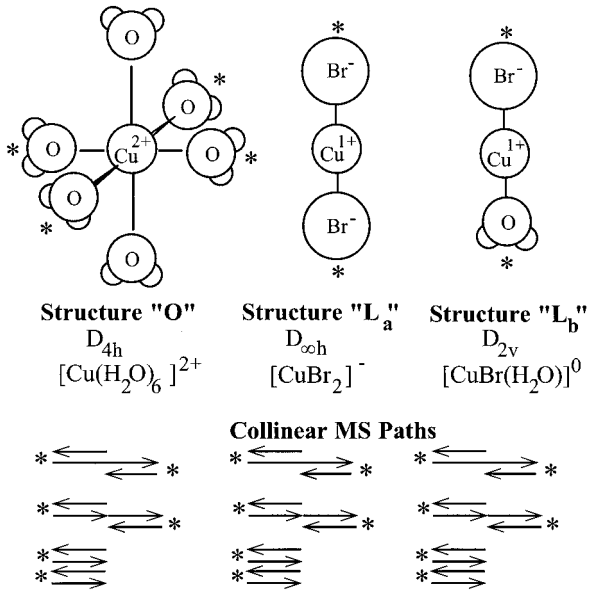

Figure 1. Schematic structures of the Cu^{2+} and Cu^{1+} hydrothermal species. The waters of hydration about the Br^- are not shown for clarity. Also depicted are the photoelectron multiple scattering paths that were used in the EXAFS analysis.

As discussed below in the XAFS analysis, the following copper redox chemistry was found to occur under hydrothermal conditions.

$$[Cu(H_2O)_6]^{2+} + 4Br^- + Cu^0 \xrightarrow{T > 100\ °C} 2[CuBr_2]^- + 6H_2O \quad (4)$$

$$[Cu(H_2O)_6]^{2+} + 2Br^- + Cu^0 \xrightarrow{T > 100\ °C} 2[Cu(H_2O)Br] + 4H_2O \quad (5)$$

and

$$2[Cu(H_2O)_6]^{2+} + (m+4)Br^- + Pt^0 \xrightarrow{T > 100\ °C} 2[CuBr_2]^- + [PtBr_m(H_2O)_n]^{(2-m)} + (6-n)H_2O \quad (6)$$

The reactions in eqs 4 and 5 were explored in the copper, microreactor batch XAFS cell, whereas the reaction in eq 6 was conducted in the Pt−Ir flow cell. While the hexaaqua Cu^{2+} species is very soluble at all temperatures, the dibromo Cu^{1+} species is only soluble at elevated temperatures. Under hydrothermal conditions Cu^{2+} acts as a strong oxidizing agent readily oxidizing Cu^0 and is even capable of oxidizing Pt^0 under the stabilizing effects of the Br^-. The presence of Br^- promotes the oxidation of Pt^0 possibly through the stabilizing effects of the new bromo copper(I) and bromo platinum(II) complexes. Although we do not have any direct experimental evidence available, tabulated standard electrochemical half-cell potentials indicate that the oxidation of Pt metal would probably proceed to Pt^{2+} rather than Pt^{4+} as shown in eq 6.

The proof of Pt oxidation comes from the observation of corrosion, the existence of Pt in effluent, and the formation of Cu(I) compounds as determined from XAFS analysis. Upon disassembly of the platinum cell, internal pitting corrosion was observed. Analysis of the cell effluent by X-ray fluorescence showed existence of both copper and platinum compounds. From the analysis of the strong $1s \rightarrow 4p$ XANES peak, we determined that in many instances there was 100% conversion of the Cu(II) to Cu(I) since the $1s \rightarrow 4p$ peak is an immediate and definitive indication of the oxidation state of the Cu. For systems involving the chemistry of eq 6, the XAFS-measured solutions contained not only complexed Cu^{1+} but also a soluble Pt^{2+} species at a lesser concentration. There is no evidence from the XAFS data for the association of the copper and platinum species under these conditions.

The following chemistry was found to occur in Cu^{2+} solutions containing nitrate ions, in the absence of bromide ions, at temperatures up to about 350 °C

$$[Cu(H_2O)_6]^{2+} + m(NO_3^-) \xrightarrow{350\ °C > T > 100\ °C} [Cu(H_2O)_{6-n}(NO_3)_m]^{2-m} + nH_2O \quad (7)$$

at higher temperatures the following dehydration reaction occurs

$$[Cu(H_2O)_6]^{2+} \xrightarrow{T > 400\ °C} CuO + 2H_3O^+ + 3H_2O \quad (8)$$

The presence of nitrate ions instead of bromide ions helps stabilize the Cu^{2+} species at high temperatures but produces Cu(II)O through dehydration reactions at temperatures above 400 °C. Indeed, the copper(II) nitrate solutions were found to remain stable at 325 °C for long times. At higher temperatures, e.g., above 400 °C, a reaction was observed during the XAFS experiment involving the formation of a solid phase. This solid is consistent with the formation of CuO.

The emphasis of this study is to determine the detailed structure of the Cu^{2+} and Cu^{1+} species illustrated in Figure 1 under hydrothermal conditions. In the following section, we show that the reactions outlined in eqs 4−8 are strongly supported by the preedge and XANES spectra. These two spectral regions give key information about the oxidation state and the coordination symmetry of the new hydrothermal species. After discussing these near-edge characteristics we move on to the extended X-ray absorption region to obtain detailed structural information about the first solvation shell.

Preedge and XANES Spectra. *Aqueous Cu^{1+} Species.* Figure 2a shows the preedge and XANES region for two aqueous solutions, one containing the hexaaqua Cu^{2+} species at room temperature and the other containing a bromo-coordinated Cu^{1+} species at high temperature. For comparison to the aqueous Cu^{1+} species, the spectra of the two solid Cu(I) reference compounds, CuBr and Cu_2O are also presented. One can readily observe the dramatic transition in the XANES structure upon heating the Cu^{2+} solution in the high-pressure XAFS cell where the reactions according to eqs 4 and 6 occur. The dominant XANES peak of the Cu(I) species at about 8982 eV is assigned to the $1s \rightarrow 4p$ transition. The high-intensity of this XANES peak means that the majority of the Cu is in the Cu^{1+} state under these conditions. The decrease in the intensity of the XANES peak at 8996 eV observed for the Cu^{2+} solution relative to that for the Cu^{1+} solution, is consistent with the removal of all tightly bound water in the first shell and the formation of a new coordination structure with only Br^-. The nature of this behavior is explained in more detail during the analysis of the amplitude functions for full EXAFS region that is presented in later sections, in which we verify the loss of tightly bound water and the formation of tightly bound Br^- ligands.

In a systematic study of 19 Cu(I) compounds, Kau et al.[31] showed that the intensity and position of the Cu(I) peak at ca. 8982 eV is strongly correlated with the degree of coordination. Kau showed that the normalized amplitudes of this XANES peak are about 1.08, 0.63 and 0.72 for the 2, 3 and 4 coordinate Cu(I) species, respectively. In addition, the Cu(I) XANES peak for 4-coordinate Cu(I) species is shifted almost 2 eV above that

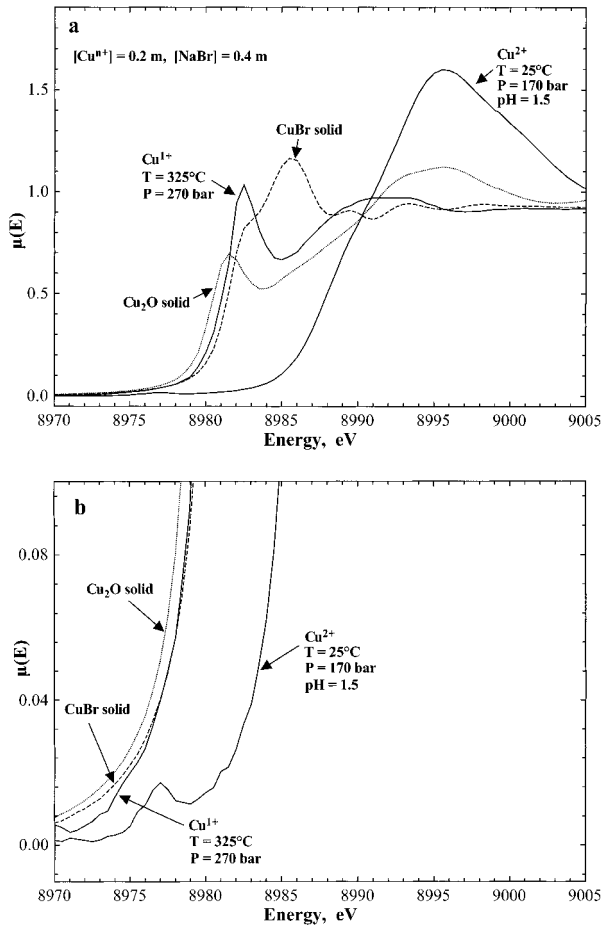

Figure 2. Preedge and XANES spectra at the Cu *K*-edge for two solutions and two solid standards. The solution spectra contain 0.2 *m* $CuBr_2$ and 0.4 *m* NaBr. *m* HBr is added to these solutions to produce a pH of 1.5 under ambient conditions. For the spectrum taken at 325 °C the Cu^{2+} has been reduced to Cu^{1+}. The reference compounds are Cu^{I}_2O and $Cu^{I}Br$ solids. The spectra in (a) show the full range of data whereas in (b) the vertical scale is expanded to show the $1s \rightarrow 3d$ transition that is only present in the solution spectra taken at 25 °C. All spectra were scaled to a common edge-height.

for the 2- and 3-coordinate Cu(I). Thus, the high-temperature solution spectra (e.g., Figure 2a) for the new Cu^{1+} species strongly indicate that this is a 2-coordinate species, since the normalized peak intensity is about 1.05, and the peak position is also consistent with a lower, 2-coordinate species. The anomalous behavior of the amplitude of the 2-coordinate solid Cu_2O in this scheme has been previously noted.[31,32] Recent images of the charge density map for Cu_2O show the existence of covalent bonding between Cu−O *and* Cu−Cu for this material.[33] Thus the delocalized electrons for Cu_2O greatly alter the nature of this transition. The solid CuBr has tetrahedrally coordinated Br^- and the higher energy of the $1s \rightarrow 4p$ at 8986 eV band is consistent with the qualitative relationship given by Kau for four-coordinate Cu(I) compounds, however the intensity of this band does not agree with this qualitative relationship.[31]

To illustrate the $1s \rightarrow 3d$ transition present only in the hexaaqua Cu^{2+} species, Figure 2b shows the preedge region on an expanded scale. Although this transition is formally dipole forbidden, it is weakly allowed through either quadrupolar [34] coupling or a slight amount of thermal disorder−mixing in *p*-character distortion to destroy the inversion symmetry. The Cu^{1+} state has a closed shell configuration (d^{10}) and thus zero probability of a $1s \rightarrow 3d$ transition. Thus, neither the solid Cu_2O nor solid CuBr show evidence of this transition. Likewise the $Cu^{1+}Br^{n+}$ solution spectrum shows no evidence of this transition and supports the analysis that the solution species at 325 °C is predominately Cu^{1+}. Further convincing evidence of the conversion of Cu^{2+} to Cu^{1+} comes from the large shift (>5 eV) in the position of the absorption edge near 8987 eV after heating. This difference in edge position is typically observed between Cu(II) and Cu(I) species.

Aqueous Cu^{2+} Species. In the presence of NO_3^- (and the absence of Br^-), the intial Cu^{2+} oxidation state is stable even at high temperatures. Figure 3 shows the XANES region for a 0.2 m $Cu(NO_3)_2$ solution at 170 bar and at three different temperatures, 25 , 200, and 325 °C. There are three important features in these XANES spectra represented by the shoulders or small peaks in the spectra of Figure 3a at 9000, 9010, and 9040 eV. These features are due to collinear multiple scattering (MS) contributions from the four, rigidly bound, equatorial water molecules.[35] This would be expected from the D_{4h} symmetry typically observed for the hexa-aqua Cu^{2+} species. At 200 °C, these MS peaks are virtually unchanged from those observed in the ambient spectra. Thus, the tetragonally distorted octahedral structure persists at 200 °C. Even at 325 °C there is evidence of the MS contribution, although the intensity at 9010 eV is somewhat diminished. An enlarged view of the preedge and XANES region is shown in Figure 3b, and the first derivatives of these spectra are given in Figure 3c. The changes in these first derivative spectra are consistent with some small changes in the coordination structure. Possible explanations include association with the NO_3^- counterion, interaction with OH^- or thermal disruption of the hexaaqua, octahedral symmetry. At 325 °C there are indications from the EXAFS spectrum (presented later) that there is some formation of small amounts of Cu(II)O and this has a significant effect on the derivative spectra around 8983 eV. Figure 3d shows the expanded view of the $1s \rightarrow 3d$ transition for the same three temperatures. Again, the 25 °C and 200 °C spectra are nearly identical in peak position and amplitude. At 325 °C, the $1s \rightarrow 3d$ band broadens to higher energy. Pickering et al.[34] have provided a detailed analysis of the assignment of this band from a study of the polarized single-crystal spectra of $CuCl_2 \cdot 2H_2O$. For an out-of-plane rotation, the $1s \rightarrow 3d$ peak was observed to move by about 1 eV to lower energy. They proposed that this was due to $d\pi - d\pi$ bonding between copper and the chloride ligand. In the current system, it is entirely possible that the onset of some $Cu^{2+}-NO_3^-$ ion pairing occurs at this temperature. It is also possible that changes in this band are due to formation of a slight amount of copper oxide or copper hydroxide or to an increase in the Cu−O distance disorder.

For the $Cu(NO_3)_2$ solutions, the Cu^{2+} ion remains stable in oxidation state and symmetry up to 325 °C. Above this temperature, a reaction occurs to form a partially insoluble solid. The preedge and XANES spectra of this decomposition product, shown in Figure 4, were acquired from the 0.2 m $Cu(NO_3)_2$ solution at temperatures of 425 °C and 525 °C. The quality of the spectra is much reduced in part due to the presence of the solid crystalline phase (evidenced by Bragg peaks in the EXAFS spectra from large crystallites) that has formed on the window surfaces at these temperatures. These spectra may also contain small contributions from soluble Cu species although the XAFS analysis tends to indicate a majority CuO phase. The new oxide material that forms is nearly identical to that of solid Cu(II)O which is shown for comparison. Analysis of the full EXAFS spectra (not shown) is also consistent with nearly complete conversion to CuO. The same solution was cooled to 325 °C

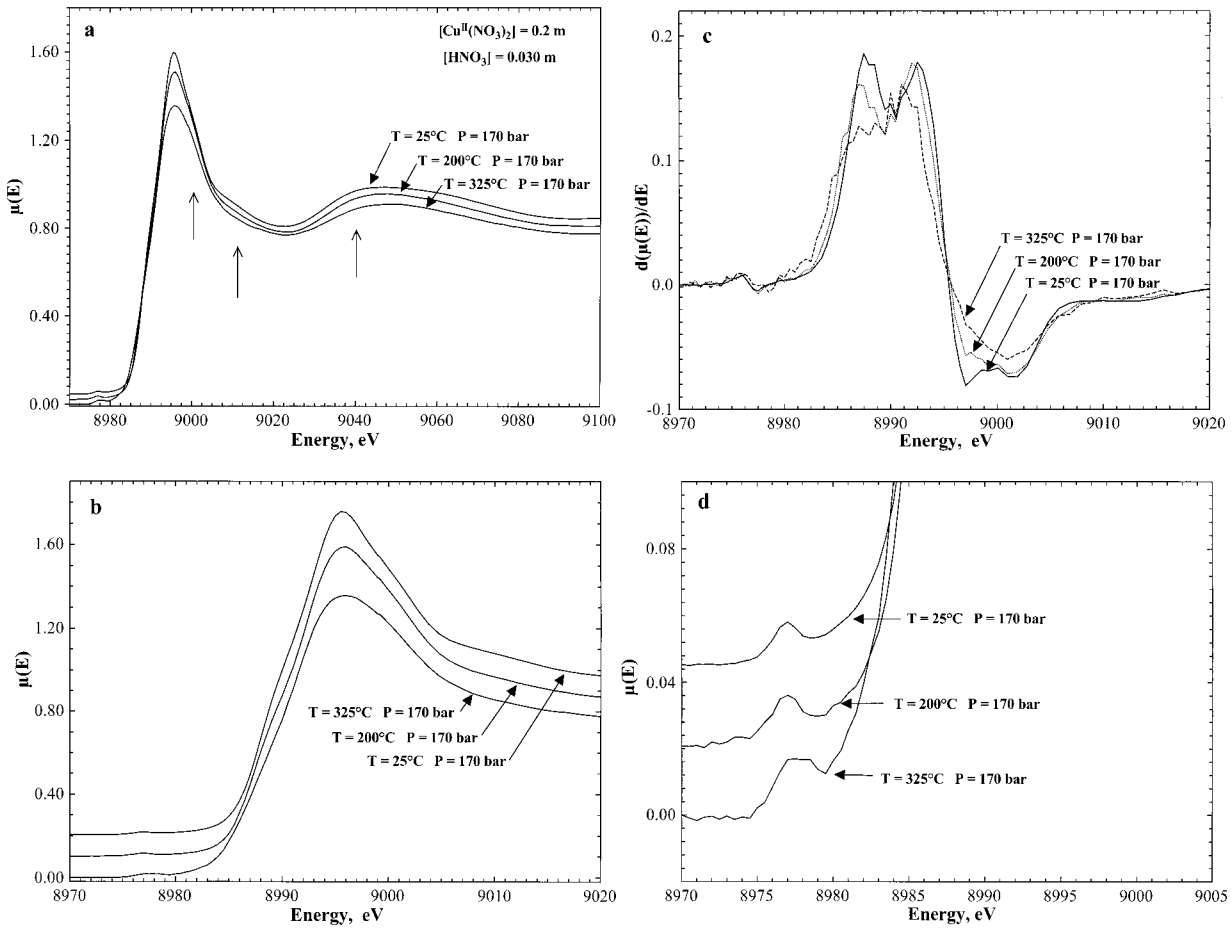

Figure 3. Preedge and XANES spectra at the Cu *K*-edge for a 0.2 *m* $Cu^{II}(NO_3)_2$ and 0.03 *m* HNO_3 solution at three temperatures from 25 °C to 325 °C. The vertical arrows in (a) indicate features from the multiple scattering contributions of the four rigidly bound equatorial waters. In (b) the edge region is expanded, in (c) the first derivative of the expanded region is shown and in (d) the $1s \rightarrow 3d$ transition region is expanded. All spectra were scaled to a common edge-height and then offset (except in (c)) for ease of viewing.

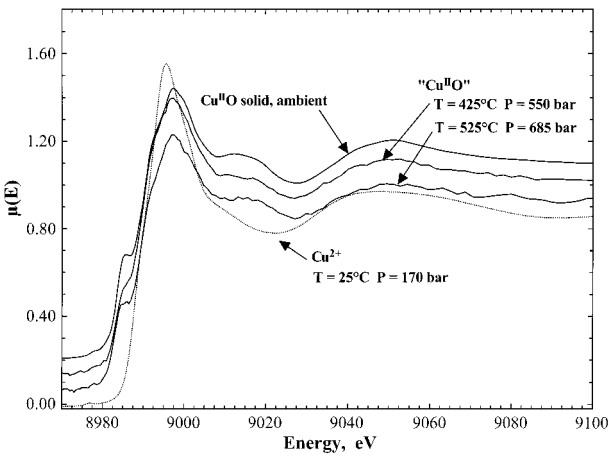

Figure 4. Preedge and XANES spectra at the Cu *K*-edge of the decomposition product of the 0.2 *m* $Cu^{II}(NO_3)_2$ and 0.03 *m* HNO_3 solution at 425 °C and 525 °C. Also shown are the reference spectra for the 0.2 *m* $Cu^{II}(NO_3)_2$ solution at 25 °C and for a solid Cu(II)O powder sample. All spectra were scaled to a common edge-height and then offset for ease of viewing.

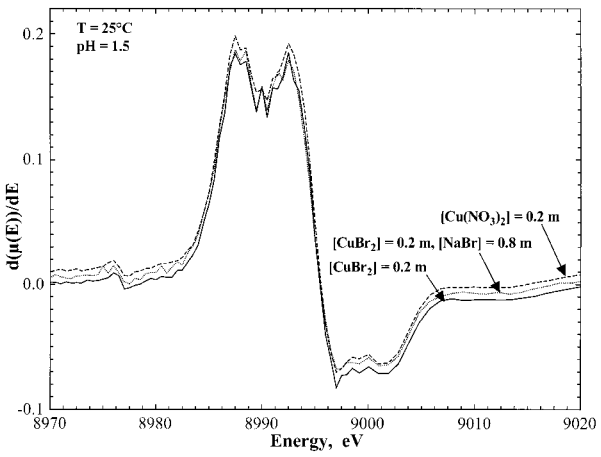

Figure 5. Derivatives of the XANES spectra for three different Cu^{2+} solutions at 25 °C. Each spectrum is offset by 0.005 units for clarity

but the solid phase irreversibly remained in the XAFS cell and we did not recover the Cu^{2+} solution spectra.

Finally, as indicated by D′Angelo et al.[12] for $CuCl_2$ solutions, small changes in the XANES spectra, that are more easily visualized in a derivative plot, are a sensitive indicator of changes in the first shell coordination. Figure 5 shows plots of the first derivatives of the XANES spectra for three different solutions at 25 °C containing 0.2 m $CuBr_2$, 0.2 m $Cu(NO_3)_2$ and 0.2 m $CuBr_2$ with 0.8 m NaBr. For the concentrations used in this study, with the two different counterions, it is apparent from the similarities of these derivative spectra that there is no significant association of these anions with the Cu^{2+} at room temperature. The solution that contains both 0.2 m $CuBr_2$ and 0.8 m NaBr shows a very slight difference in the amplitudes between 8985 and 9005 eV. This is a possible indication of a slight amount of association of the Br^- with Cu^{2+} at room temperature. In contrast, higher temperatures will drive the

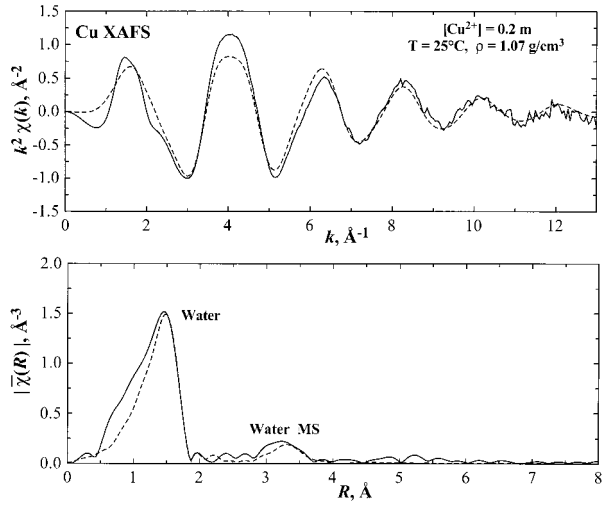

Figure 6. A Cu EXAFS k^2-weighted $\chi(k)$ plot (top) for a 0.2 m $CuBr_2$ solution at 25 °C and 170 bar. The sole species is the hexaaqua Cu^{2+}. The solid line shows the experimental data and the dashed line shows the model fit to the data using FEFF calculations and the parameters listed in Table 2. The Fourier transform (bottom) of the $\chi(k)$ data reveals the position of the water in the first shell and the contribution from multiple scattering from the four equatorial waters. This $|\tilde{\chi}(R)|$ plot is uncorrected for phase shifts, whereas the corrected distances are reported in Table 2.

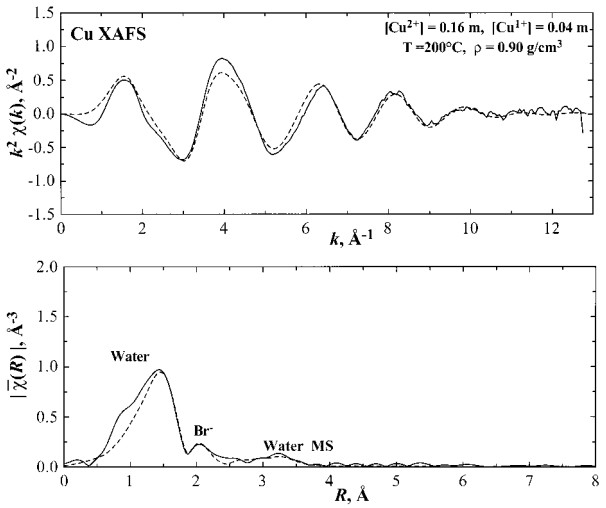

Figure 7. A Cu EXAFS k^2-weighted $\chi(k)$ plot (top) for a $CuBr_n$ solution containing 0.16 *m* Cu^{2+} and 0.04 *m* Cu^{1+} at 200 °C and 170 bar. The solid line shows the experimental data and the dashed line shows the model fit to the data using FEFF calculations and the parameters listed in Table 2. The Fourier transform (bottom) of the $\chi(k)$ data reveals the positions of the water and Br^- in the first shell and the contribution from multiple scattering from the four equatorial waters. This $|\tilde{\chi}(R)|$ plot is uncorrected for phase shifts whereas the corrected distances are reported in Table 2.

association of Cu^{2+} with the respective counterions as is discussed in the following sections.

EXAFS Spectra and the Fitted Results. *Overview.* In the following sections, information extracted from the EXAFS region is used to further refine the structure of the hydrothermal Cu^{1+} and Cu^{2+} species present under hydrothermal conditions. The first group of experiments involve different Cu/Br ratios to explore the structure of the Cu^{1+} species and to illustrate the Cu(I)/Cu(II) equilibrium at lower temperatures. For two of these Cu/Br systems at 325 °C, both Cu and Br EXAFS are acquired to obtain the highest quality details of the coordination structure. The second group of experiments involves the Cu/NO_3^- system in which we explore the high-temperature coordination structure of the Cu^{2+} state.

Figures 6, 7, 8, 9, and 11 present k^2-weighted $\chi(k)$ data at the Cu *K*-edge for various copper solutions from 25 °C to 325 °C. Figures 9 and 11 also present the Br *K*-edge spectra. In all cases, the usable *k*-range extends out to about 13 $Å^{-1}$. Figures 10 and 12, and the bottom plots in Figures 6, 7, and 8 give the $\tilde{\chi}(R)$ results or the magnitude of the Fourier transformed $\chi(k)$ data. The $\tilde{\chi}(R)$ functions represent the radial, partial-pair distribution functions that are convoluted with the photoelectron scattering functions as shown in eq 1. The dashed lines in all cases represent the theoretical fits to the experiment data using the theoretical standards derived from FEFF. The tabulated values for all of the fitted parameters defining the various partial-pair distribution functions are reported in Tables 2−4.

Most of the systems in Tables 2−4 contained either pure Cu^{2+} or pure Cu^{1+}. Two of the systems reported in Table 2 contained mixed oxidation states. In all cases, the approximate structures are indicated by the nomenclature defined in Figure 1 as "**O**" for distorted octahedral, "$\mathbf{L_a}$" for the linear dibromo species and "$\mathbf{L_b}$" for the linear monoaqua-monobromo species. The percentages of Cu^{2+} and Cu^{1+} reported in the second column of Table 2 were obtained from the analysis of the XANES peak at 8982 eV. The amounts of soluble Cu or Br were determined from the height of the absorption edges and from the known absorption cross sections. In most cases, the amount of soluble Cu

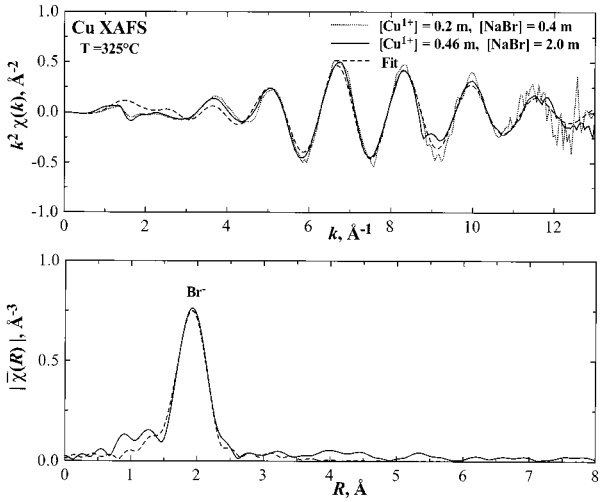

Figure 8. A Cu EXAFS k^2-weighted $\chi(k)$ plot (top) for two different Cu^{1+} solutions. On contains 0.2 *m* Cu^{1+} and 0.4 *m* NaBr (dotted line), the other contains 0.46 *m* Cu^{1+} and 2 *m* NaBr (solid line). Both solutions are at 325 °C. The dashed line shows the model fit to the data using FEFF calculations and the parameters listed in Table 2. The Fourier transform (bottom) of the $\chi(k)$ data reveals the position of the Br^- in the first shell. This $|\tilde{\chi}(R)|$ plot is uncorrected for phase shifts whereas the corrected distances are reported in Table 2.

was equal to the amount of added Cu. The measurements of the samples with the mixed oxidation states may not be the equilibrium distribution although reaction rates appear to be very fast at these temperatures. Further, we know that there is no change in the chemistry over the course of an EXAFS scan, since a second EXAFS scan that is acquired 20 min later is identical to the first. For those samples that contain excess Br^-, the reaction heavily favors formation of the bromo Cu^{1+} species.

The series of spectra shown in Figures 6, 7, and 8 illustrate the transition from Cu^{2+} coordination at 25 °C to Cu^{1+} at 325 °C. For the 25 °C spectra the hexaaqua copper(II) species is observed (in the Pt−Ir cell). As the temperature is increased, two significant changes occur. First, the Cu^{2+} is reduced to Cu^{1+}

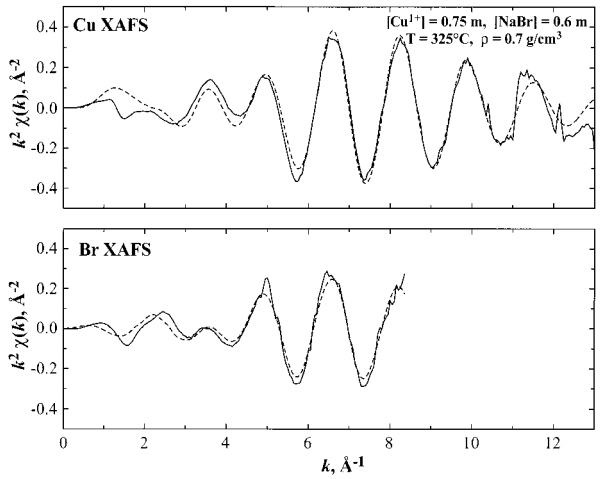

Figure 9. k^2-weighted $\chi(k)$ plot (top) plots for Cu and Br^- EXAFS under hydrothermal conditions for a solution containing 0.75 *m* Cu^{1+} and 0.6 *m* NaBr at 325 °C. The solid line shows the experimental data and the dashed line shows the global model fit to both data sets using FEFF calculations and the parameters listed in Table 4. The Br $\chi(k)$ data does not extend beyond $k = 8.5$ in this case.

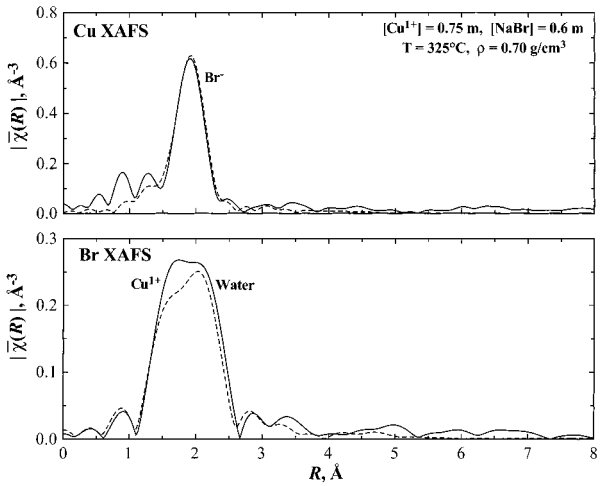

Figure 10. The $|\tilde{\chi}(R)|$ plot from the spectra shown in Figure 9 for the solution containing 0.75 *m* Cu^{1+} and 0.6 *m* NaBr at 325 °C. The solid line shows the experimental data and the dashed line shows the global model fit using FEFF calculations and the parameters listed in Table 4. The $|\tilde{\chi}(R)|$ plot is uncorrected for phase shifts whereas the corrected distances are reported in Table 4.

through a redox reaction with Cu^0 or Pt^0 (eqs 4−6) as monitored by the XANES peak intensity. Second, there is increasing association of the Br^- in the first shell about the Cu as shown in the $\tilde{\chi}(R)$ plot of Figure 7. Another significant aspect of the $\tilde{\chi}(R)$ plot in Figure 7 is the feature at about 3.3 Å due to the multiple scattering contributions of the strongly bound equatorial ligands. For the system containing Br^-, the reduction in the intensity of the MS peak at higher temperature is due in part to the formation of $Cu(I)Br_2^-$ species but may also be due to disruption of the hexaaqua octahedral Cu^{2+} species through formation of $[Cu(II)Br_m(H_2O)_n]^{2-m}$ species. In the next section, we evaluate the EXAFS spectra of those systems containing only Cu^{1+} and then, in a subsequent section, we evaluate the Cu^{2+} structure.

Aqueous Cu^{1+} Species. For the 325 °C spectra shown in Figure 8, Cu^{1+} is the only species present. The figure includes spectra for two different Cu and NaBr concentrations, one has a moderate salt concentrations (0.2 *m* Cu^{1+} and 0.4 *m* NaBr) the other has a large excess of NaBr (0.46 *m* Cu^{1+} and 2 *m* NaBr). The interesting result is that these two spectra are nearly identical, strongly indicating that there are no increases in the coordination even with very high Br^- concentrations. The coordination numbers for both of these systems reported in Table 2, are 2.1 and 2.2, respectively. These coordination numbers are, within experimental error, equivalent to the "$\mathbf{L_a}$" dibromo Cu^{1+} species illustrated in Figure 1. What is more, the peak height of the $1s \rightarrow 4p$ transition in the XANES region for these two solutions are the same, further strongly reinforcing the conclusion that the highest coordination species is the dibromo Cu^{1+} even for high NaBr concentrations under conditions that might be expected to favor higher Br^- coordination.

It is instructive to compare the very different nature of the $\chi(k)$ plot for the 325 °C, Cu^{1+} species in Figure 8 with the hexaaqua Cu^{2+} species given in Figure 6. Since bromine is a much higher Z atom than oxygen, the amplitude and phase functions ($F(k)$ and $\delta(k)$ in eq 1) derived from FEFF for bromine have significantly different features than those for oxygen. For bromine, the $F(k)$ function has a large amplitude for $k > 5$ Å^{-1}, whereas for oxygen the $F(k)$ function is most significant at $k <$

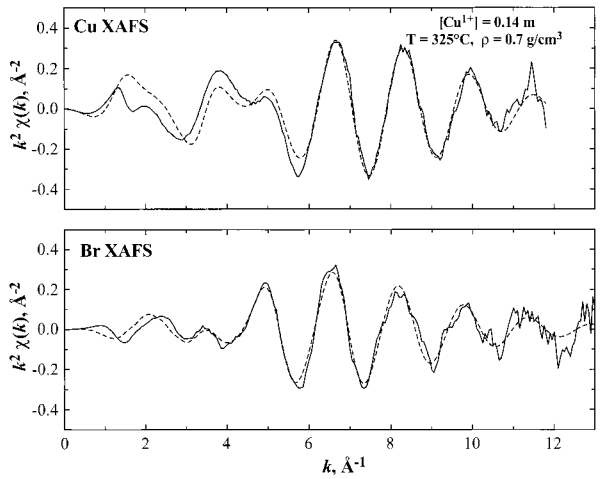

Figure 11. k^2-weighted $\chi(k)$ plots for Cu and Br^- EXAFS under hydrothermal conditions for a solution containing 0.14 *m* Cu^{1+} at 325 °C. The solid line shows the experimental data and the dashed line shows the global model fit to both data sets using FEFF calculations and the parameters listed in Table 4.

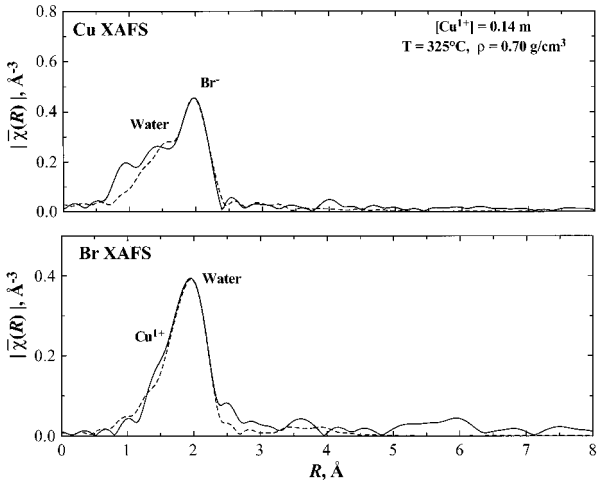

Figure 12. The $|\tilde{\chi}(R)|$ plot from the spectra shown in Figure 9 for the solution containing 0.14 *m* Cu^{1+} at 325 °C. The solid line shows the experimental data and the dashed line shows the global model fit using FEFF calculations and the parameters listed in Table 4. The $|\tilde{\chi}(R)|$ plot is uncorrected for phase shifts whereas the corrected distances are reported in Table 4.

TABLE 2: Cu(I,II) Speciation under Slightly Reducing Hydrothermal Conditions. Results of Cu XAFS Analysis of First-Shell Cu(I,II) Structures[a]

system						conditions			structure				
ID	species	$[Cu^{2+}]$	$[Cu^{1+}]$	[NaBr]	[HBr]	*T*, °C	P, bar	ρ, g/cm^3	scatterer	*N*	*R*, Å	$\sigma^2 \times 10^3$, Å^2	$C_3 \times 10^4$
A	**O**	0.2	0.0	0.0	0.03	25	170	1.07	oxygen	4.0(0.4)[b]	1.971(012)	5.2(1.1)	1.1(2.5)
									oxygen	2[c]	2.385(045)	27.5(11.5)	
B	**O**	0.2	0.0	0.8	0.03	25	170	1.12	oxygen	3.7(0.4)[b]	1.970(010)	4.2(0.9)	0.4(2.0)
									oxygen	2[c]	2.388(045)	29.9(11.7)	
C	20%**L** & 80%**O**	0.16	0.04	0.0	0.03	200	170	0.90	bromine	0.8(0.4)	2.321(010)	10.5(3.1)	
									oxygen	3.3(0.6)[b]	1.974(055)	9.4(2.2)	
D	90%$\mathbf{L_a}$ & 10%**O**	0.02	0.18	0.8	0.03	200	170	0.92	bromine	1.9(0.3)	2.293(019)	7.5(1.2)	2.0(3.6)
									oxygen	0.3(0.7)[b]	2.005(058)	5.1(29.6)	
E	$\mathbf{L_a}$ & $\mathbf{L_b}$	0.0	0.02[d]	0.0	0.03	200		0.90	bromine	1.6(0.3)	2.276(023)	7.7(1.8)	0.0(5.0)
									oxygen	0.4(0.3)	1.965(025)	3.4(13.3)	
F	$\mathbf{L_a}$	0.0	0.44	2.0	0.08	200		0.90	bromine	2.1(0.3)	2.335(009)	10.3(1.0)	5.9(1.8)
G	$\mathbf{L_a}$	0.0	0.2	0.4	0.03	325	270	0.69	bromine	2.1(0.2)	2.268(004)	7.4(0.5)	0.8(0.8)
H	$\mathbf{L_a}$	0.0	0.46	2.0	0.08	325		0.72	bromine	2.2(0.2)	2.290(006)	8.6(0.7)	3.4(1.2)

[a] The predominant species types (**O**, $\mathbf{L_a}$, or $\mathbf{L_b}$) are shown in Figure 1. The concentrations represent those at the reported conditions and they are expressed in molality. The reported amounts of soluble Cu^{2+} and Cu^{1+} were determined from the edge and preedge peak heights at the stated conditions. Experiments "A", "B", "C", "D", and "G" were conducted in the Pt−Ir cell and samples "E", "F" and "H" were conducted in the Cu cell. In all cases the starting solution contained $CuBr_2$ salt that adds additional available Br^- according to the reactions in eq 4−6. [b] Fit includes multiple scattering paths for equitorial oxygens as depicted in Figure 1. [c] Fixed in the fitting. [d] Only 5% of total added Cu is soluble under these conditions.

TABLE 3: Cu(II) Speciation under Slightly Oxidizing Hydrothermal Conditions. Results of Cu XAFS Analysis of First-Shell Cu(II) Structures[a]

system				conditions			structure				
ID	species	$[Cu^{II}(NO_3)_2]$	$[HNO_3]$	*T*, °C	P, bar	ρ, g/cm^3	scatterer	*N*	*R*, Å	$\sigma^2 \times 10^3$, Å^2	$C_3 \times 10^4$
I	**O**	0.2	0.03	25	170	1.05	oxygen	3.8(0.5)[b]	1.969(017)	4.5(1.5)	1.4(3.8)
							oxygen	2[c]	2.413(072)	35.6(22.0)	
J	**O**	0.2	0.03	200	170	0.89	oxygen	4.0(0.7)[b]	1.970(015)	7.3(1.9)	1.0(3.8)
							oxygen	2[c]	2.409(108)	54.8(41.9)	
K	**O** & 5%CuO	0.2	0.03	325	170	0.54	oxygen[d]	4.3(1.0)[b]	1.972(007)	10.2(3.2)	
							oxygen	2[c]	2.406(055)	31.1(18.9)	
							oxygen(CuO)	0.3(0.2)[d]	2.836(039)	0.008[e]	

[a]Concentrations expressed in molality. The predominant species type (**O**) is shown in Figure 1. These spectra were acquired in the Pt−Ir cell. [b] Fit includes collinear multiple scattering paths for equitorial oxygens as depicted in Figure 1. [c] Fixed in the fitting. [d] In addition to the aqua Cu^{2+} ion this path also contains contributions from 5% of a CuO compound. [e] Fixed to the value corresponding to solid Cu(II)O.

TABLE 4: Global Model Fit to *Both* Cu and Br XAFS Measurements. Results of XAFS Analysis for the First-Shell Cu^{1+} and the First-Shell Br^- Structure and for the $CuBr_n$ Ion Pair under Reducing Hydrothermal Conditions[a]

system					conditions			structure				
ID	species	$[Cu^{1+}]$	[NaBr]	[HBr]	*T*, °C	ρ, g/cm^3	absorber	scatterer	*N*	*R*, Å	$\sigma^2 \times 10^3$, Å^2	$C_3 \times 10^4$
M	90%$\mathbf{L_a}$	0.75	0.6	0.03	325	~0.7	copper	bromine	1.9(0.2)	2.307(006)	8.7(0.6)	4.8(1.1)
								oxygen	0.2(0.9)	2.077(043)	10.0[b]	
							bromine	copper	1.1(0.2)[d]	2.307(006)	8.7(0.6)	4.8(1.1)
								oxygen	2.4(0.8)	3.269(037)	35.0[f]	
N	$\mathbf{L_b}$	0.14[c]	0.0	0.03	325	~0.7	copper	bromine	1.6(0.2)	2.279(010)	9.9(0.9)	1.0(1.7)
								oxygen	0.4(0.1)	1.961(013)	3.9(3.7)	
							bromine	copper	1.3(0.1)[e]	2.279(010)	9.9(0.9)	1.0(1.7)
								oxygen	3.1(1.1)	3.223(040)	35.0[f]	

[a] Concentrations expressed in molality. The predominant species of types $\mathbf{L_b}$ and $\mathbf{L_a}$ are shown in Figure 1. The Cu−Br shared parameters in the global fit are *N*, *R*, σ^2, and C_3. These experiments were conducted in the Cu cell. In both cases the starting solution contained $CuBr_2$ salt that adds additional available Br^- according to the reactions in eqs 4 and 5. [b] Due to the low extent of water coordination for this system, the Debye−Waller factor was fixed based upon previous measurements (see Table 3). [c] About 35% of total added Cu is soluble under these conditions. [d] This value was fixed at $(N_{CuBr})/1.8$ based on the measured total dissolved Cu and Br from edge height determination. [e] This value was fixed at $(N_{CuBr})/1.2$ based on the measured total dissolved Cu and Br from edge height determination. [f] Due to the low extent of water coordination for this system, the Debye−Waller factor was fixed based upon previous measurements.[17]

5 Å^{-1}. Thus the oscillations in Figure 8 arise solely from the associating Br^- and not from water. If even one or two waters (oxygens) were present about the Cu^{1+} species one should see large amplitude oscillations between $1 < k < 5$ Å^{-1} as is seen for the hexaaqua species in Figure 6. Note also the different vertical scales in these two figures. These qualitative observations from the $\chi(k)$ plot are born out in the fitted results (tabulated results in Table 2). The inclusion of scattering paths for first shell water had no effect on the quality of the fits for these two systems. The lack of any significant contribution from water means that if any water is present it must be at very long distances (>3 Å) and/or it must be so weakly bound that the Debye−Waller factor would be quite large. This also positively excludes the presence of a hydrolysis species with associating OH^- since the electrostatic attraction of such a species would provide a short-range, tightly bound coordination. The complete loss of tightly bound waters for the Cu^{1+} species is different from what was observed for the $NiBr_2$ system. In the latter case, one bound water molecule (or OH^-) remained about Ni^{2+} up to 525 °C even though there were 3−4 strongly associating Br^-

in the first shell that could potentially displace them.[7] In Figure 8, the EXAFS oscillations are still strong out to $k = 13$ Å^{-1}. This means that there is low disorder in the Cu−Br association (small Debye−Waller term in eq 1) and that this species is very tightly bound.

Figures 9 and 11 present the Cu-edge *and* Br-edge k^2-weighted $\chi(k)$ plots for the 0.7 m Cu^{1+}/0.6 m NaBr and the 0.14 m Cu^{1+} solutions, respectively, at 325 °C in the Cu metal cell. As before, the XANES peak analysis of these solutions indicates that all of the Cu^{2+} has been reduced to Cu^{1+} at 325 °C. Furthermore, the Cu and Br EXAFS data were *simultaneously* fit to one global model (dashed lines) in which the shared parameters for the Cu−Br interaction are R, σ^2, and C_3. In addition, the Cu−Br and Br−Cu coordination numbers where constrained by the overall Cu/Br ratio. This global model gives an excellent fit to these two experimental conditions giving very high confidence in the extracted parameters reported in Table 4.

Figures 10 and 12 present the corresponding $\tilde{\chi}(R)$ plot from the transformed $\chi(k)$ data of copper solutions given in Figures 9 and 11. The Cu $\tilde{\chi}(R)$ plot in Figure 10 conveys a nearly unimodal Br^- peak at about 2 Å (The distances for the $\tilde{\chi}(R)$ plots in the figures are uncorrected for the EXAFS phase shifts, whereas the tabulated values of the true distances are reported in Table 4). The bimodal peak in the Br $\tilde{\chi}(R)$ plot between 1.2 and 2.7 Å contains the contributions from the copper and the remaining hydration waters in the first shell about the bromide ion. For anionic species such as Br^-, the water molecule is situated such that the proton lies between the anion and the oxygen of the water molecule and thus the Br−O distance is longer than the Br−Cu distance. In the Cu $\tilde{\chi}(R)$ plot for the solution without added NaBr in Figure 12, there is evidence of water association in the first shell about Cu^{1+}.

Solution "M" in Table 4 contains an almost stoichiometric amount of added NaBr to produce the $[CuBr_2]^-$ species. Thus, according to eq 4, the predominant species present in solution "M" is the dibromo Cu^{1+} complex ("**L$_a$**" in Figure 1). As for the previous solutions, within the experimental uncertainty, the measured number of Br about Cu is about 2 whereas the number of Cu about Br is 1 as one would expect to find for the $[CuBr_2]^-$ species. Since the Cu−Br interactions are independently measured twice (Cu EXAFS *and* Br EXAFS), accurate values of the Cu−Br distance and the third cumulant C_3 are obtained in this case. As has previously been shown for these hydrothermal ions,[17] accurate measurements of C_3 are required in order to obtain the best measure of the Cu−Br distance since these two parameters are strongly correlated.

The lack of added NaBr salt for solution "N" limits the available Br to a 1:1 molar ratio of Cu^{1+}/Br. As a result the analysis is more complicated for solution "N". As indicated in eq 5, there is a significant amount of water (or possibly OH^-) associating with the Cu^{1+}. The total average coordination about the Cu^{1+} is still two (0.4 H_2O + 1.6 Br^-). This is consistent with the XANES spectra for this solution, where the peak height of the $1s \rightarrow 4p$ transition is the same as that for all 2-coordinated Cu^{1+} species. Thus a second linear species "**L$_b$**", shown in Figure 1 is indicated. Since the Br^- coordination about the Cu^{1+} is 1.6, whereas the water coordination is only 0.4, a mixture of "**L$_b$**" and "**L$_a$**" species may be present. A second interpretation of the structure for this solution would involve a linear bromo-Cu^{1+} *dimer* species with one of the two coppers terminated with a water molecule (H_2O−Cu−Br−Cu−Br). This would satisfy the requirement of maintaining an overall 1:1 mole ratio of Cu-to-Br imposed by the simple redox chemistry ($CuBr_2 + Cu^0 \rightarrow CuBr^0$) for this solution with no added NaBr salt. Such a species would also explain the 1.6 Br^- coordination about Cu^{1+} for solutions "E" and "N" reported in Tables 2 and 4. The XANES spectra for such a dimer species would not be expected to be significantly different from that of the monomer. Also, due to the unhindered bending about the central Br, and the resulting disorder of the Cu−Cu distances, the Cu−Cu single scattering paths may not be observed.

Returning to the dibromo Cu^{1+} species ("**L$_a$**" in Figure 1), it is instructive to compare the aqueous $[CuBr_2]^-$ structure with the structural parameters found in the solid Cu(I)Br and Cu(II)Br_2 materials. For Cu(I)Br solid, the Cu−Br distance of 2.47 Å that we measure by EXAFS is within 0.02 Å of previous XAFS[36] and crystallographic data.[37] For Cu(II)Br_2 the measured Cu−Br distance is 2.45 Å. The best measure of the Cu−Br distance for the hydrothermal $Cu^{1+}Br_2^-$ species is for the system in which both the Cu and Br EXAFS were measured as reported in Table 4. At 325 °C, the measured Cu−Br distance is 2.31 Å which represents a contraction of about 0.15 Å for this ion pair distance compared to that in the solid Cu(I)Br. A similar bond distance contraction was also observed for the aqueous $NiBr_2$ system, where the ion-paired hydrothermal species $NiBr_3(H_2O)^-$ had a Ni−Br distance that was 0.14 Å shorter than for solid $NiBr_2$.[7] As we have previously indicated,[4] contraction of the bond distance results from the strong electrostatic interactions between the isolated pair of ions in hydrothermal solutions versus the more saturated electrostatic interactions in a solid in which neighboring cations share the first shell anions.

Evaluation of Multiple Scattering Contributions for the Cu^{1+} Species. A highly probable species is the linear Br^-−Cu^{1+}−Br^- structure illustrated in Figure 1. The latest XAFS scattering codes (e.g., FEFF7) provide a very high level of performance and thus one can readily test hypotheses about different coordination symmetries by comparing calculated single- (SS) and multiple- (MS) scattering paths against the measured XAFS spectra. Different types of multiple scattering contributions were explored for the Cu and Br XAFS to examine the possibility of a linear Br−Cu−Br species. The contribution to the total Cu $\chi(k)$ from the two collinear multiple scattering paths (defined in Figure 1) was found to be relatively small since the calculated amplitude ratios were about 10% of the single scattering contributions. In addition, the Br amplitude function for the multiple scattering paths does not become significant until above about $k = 5$ Å^{-1}. Thus the long distance (4.6 Å) associated with these paths means that the MS paths are strongly damped at higher k. On the other hand the situation is potentially more favorable for the Br $\chi(k)$ because of the focusing effect of the central Cu atom for the MS paths (defined in Figure 1). FEFF analysis of this contribution again indicates significant SS and MS contributions above $k = 6$ Å^{-1} although these would be substantially damped by a moderate Debye−Waller factor. Inclusion of these SS and MS paths to the fits for solution "M" in Table 4 had little effect on the quality of the fits primarily because the Cu−Br distance disorder is too large. The lack of significant multiple scattering contributions for the linear $[CuBr_2]^-$ species is in marked contrast to the behavior observed recently for the linear $[CuCl_2]^-$ species at high temperature[38] where the reduction and coordination chemistry is nearly the same as for Br^-. In the case of $[CuCl_2]^-$, the Cu−Cl amplitude functions are more favorable at low k than they are for Br and an intense MS peak is observed for the linear species in this case. In addition, the Cl^- is more tightly bound than the Br^- in part because of its smaller size. Hence, the lower disorder leads to a stronger MS contribution for the $[CuCl_2]^-$ system.

The MS analysis was also applied to the high-temperature Cu^{1+} solution that had no added NaBr (solution "N" in Table 4). The model included all SS and MS contributions from the linear dimer species $H_2O-Cu^{1+}-Br^{-}-Cu^{1+}-Br^{-}$. In this case, a slight improvement in the overall fit was obtained, especially for the small peak at 4 Å in Figure 12 that is tentatively assigned to a Cu−Cu SS path. Thus, the analysis supports the hypothesis of a linear dimer species at this concentration and temperature.

Aqueous Cu (II) Species. The fitting procedure for the room-temperature octahedral structure of the hexaaqua Cu^{2+} was similar to that previously reported by D′Angelo et al.[12] and Korshin et al.[13] As in this prior work, we found that the collinear multiple scattering paths of the equatorial waters provide a significant contribution to the $\chi(k)$ data. Inclusion of a second water solvation shell at about 3.4 Å having the structure reported by D′Angelo et al. slightly improved the fit to the experimental data in the region from $2 < k < 5$ Å^{-1}. At higher temperatures this contribution was insignificant. In the fitting process for the room-temperature hexaaqua species, the number of axial waters was fixed at 2, all other parameters were derived from the EXAFS data. There is excellent agreement with distances (±0.5%) and Debye−Waller factors (±20%) for the equatorial waters previously reported by D′Angelo et al.[12] Last, considering the large amount of disorder for the axial water ligands, our measurements of $R_{axial} = 2.39$ Å and $\sigma^2_{axial} = 0.03$ are also in reasonable agreement with this prior work which reported $R_{axial} = 2.29$ Å and $\sigma^2_{axial} = 0.02$.

Table 3 reports the effect of temperature on the coordination structure of the Cu^{2+} species in the presence of nitrate ions. At 200 °C the distorted octahedral structure remains intact with no detectable changes in the coordination structure. At 325 °C small structural changes have occurred. The radial structure plot ($\tilde{\chi}(R)$, not shown) for the $Cu(NO_3)_2$ solutions at 325 °C still has a prominent MS peak at about 3.2 Å. Correspondingly, the XANES spectra in Figure 3a still shows evidence of MS contributions. At this temperature, there is indication of the presence of a small amount (<5%) of a CuO compound, and we know that at 425 °C there is nearly complete conversion of the hexaaqua Cu^{2+} to Cu(II)O. The fits to the first shell structure for the 325 °C spectra include paths assigned to CuO. The existence of small amounts of CuO at 325 °C complicates the analysis of these data but some general observations are clear. No large changes in the hexaaqua structure occur at 325 °C, since the distances and coordination numbers are nearly the same as for the lower temperature case. The existence of octahedral symmetry for Cu^{2+} at 325 °C was also observed for the hexaaqua Ni^{2+} in an earlier study[7] although at 425° this structure was destroyed.

For the EXAFS spectra taken at 325 °C (solution "K"), it is more difficult to deconvolute the different possible species quantitatively. The fitting approach entails inclusion of a small amount of CuO species that we know from the XANES and EXAFS spectra is the final state of the Cu at temperatures above 400 °C. For the 325 °C spectrum, it is not possible to entirely exclude the existence of small amounts of other species such as $Cu(NO_3)^{1+}$ and $Cu(OH)^{1+}$. At higher temperatures, electrostatic attraction would favor the formation of a contact ion pair consisting of the Cu^{2+} with anionic species such as NO_3^- or OH^-. In the case of NO_3^-, a strongly bonded contact-ion pair would lead to additional backscattering contributions from the nitrogen atom in NO_3^-. There is no evidence of this type of species at 200 °C although as indicated earlier, changes in the XANES spectra could be due to weak associations with NO_3^-, perhaps at the axial ligand site. With XAFS there is no way to differentiate an O atom of H_2O from that of a OH^-. Thus, we cannot positively exclude the existence of a hydrolysis species such as $Cu(OH)(H_2O)_n^{1+}$ although this species is unlikely for the following reasons. First, the starting solution is moderately acidic which disfavors this type of equilibria. Second, the $Cu^{2+}-OH^-$ interaction would be expected to be at an appreciable shorter distance than that of the $Cu^{2+}-H_2O$ intereaction because of the additional electrostatic component. This would not only destroy the symmetry of this octahedral species and alter the nature of the $1s \rightarrow 3d$ transition but would also significantly affect the measured Cu−O bond distances and the Debye−Waller factors.

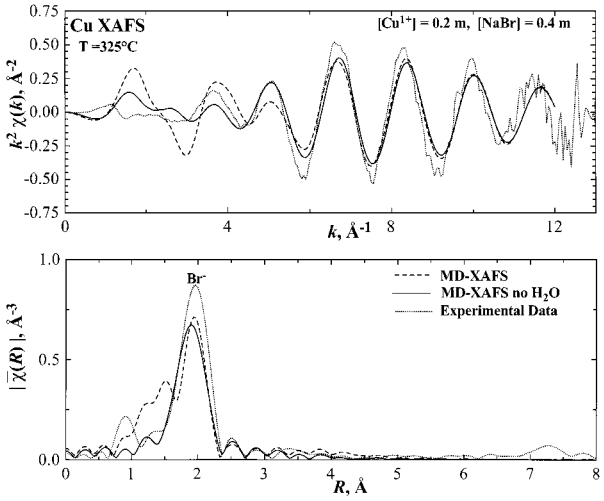

Figure 13. A Cu EXAFS k^2-weighted $\chi(k)$ plot (top) for Cu^{1+} from the MD simulation (MD-XAFS) corresponding to a solution with 0.2 m Cu^{1+} and 0.4 m NaBr at 325 °C and a density of 0.69 g/cm^3. For these simulations the N_{Br} was fixed at 2 for the duration of the simulation. The dashed line shows the MD-XAFS, the solid line shows the same MD-XAFS simulation with the water molecules removed and the dotted line shows the experimentally determined EXAFS. The bottom plot provides the $|\tilde{\chi}(R)|$ result for the three systems. The parameters extracted from fitting (FEFFIT) to both of the MD-XAFS spectra are listed in Table 5. The fitted and simulated data have been scaled by $S_0^2 = 0.85$.

Simulation Results and Discussion

Aqueous Cu^{1+} Species. Figure 13 presents the Cu-edge k^2-weighted $\chi(k)$ plots for a 0.2 m $CuBr_2$ and 0.4 m NaBr solution at 325 °C and 0.69 g/cm^3 that were generated from the MD simulation (MD-XAFS) under conditions that match solution "G". The same data reduction model that was used to extract the parameters from the experimental data was applied to the MD-XAFS spectra. The parameters from this fit are reported in Table 5. The simulated spectra in Figure 13 were calculated by both including and excluding the oxygens associated with the water molecules. It can be immediately noted that the spectrum without the oxygens does a much better job of reproducing the experimental spectrum at low k. This suggests that the simulation is doing a poor job of modeling the structure of water inside the first solvation shell of the $[CuBr_2]^-$ complex.

For the MD simulation, the initial conditions were chosen so that the number of Br^- in the first shell (N_{Br}) was equal to two. This value was chosen based on the experimental results. No restraining force was used to hold the bromines onto the Cu^{1+} ion once the initial configuration was prepared. The bromines appeared to be relatively stable and remained associated with the Cu^{1+} for the entire simulation period. Similar behavior was observed previously in simulations of $NiBr_2$ under

TABLE 5: Model Fit to Cu XAFS from MD Simulations[a]

system				conditions		structure				
ID	species	$[Cu^{1+}]$	[NaBr]	T, °C	ρ, g/cm^3	scatterer	N	R, Å	$\sigma^2 \times 10^3$, Å^2	$C_3 \times 10^4$
P	$\mathbf{L_a}$	0.2	0.4	325	0.69	bromine	1.5(0.2)	2.298(014)	6.4(0.6)	6.5(1.6)
						oxygen	1.9(0.6)	2.058(024)	29.3(12.0)	

[a]The same data reduction method (FEFFIT) was applied to the MD-XAFS that was used to recover the experimental parameters given in Table 2. Results of XAFS analysis of the first-shell Cu^{1+} hydration, and the Cu^{1+}/Br_n ion pair under hydrothermal conditions.

TABLE 6: Structural Parameters Obtained Directly from the Molecular Dynamics Pair Distribution Functions, $G_{ij}(r)$ (Figure 14)[a]

system				conditions		structure				
ID	species	$[Cu^{1+}]$	[NaBr]	T, °C	ρ, g/cm^3	atom	N	R, Å	$\sigma^2 \times 10^3$, Å^2	$C_3 \times 10^4$
P	$\mathbf{L_a}$	0.2	0.4	325	0.69	bromine	2.0[b]	2.252	8.4[d]	6.3[d]
						oxygen	1.3[c]	2.043	5.5[d]	

[a] The $G_{ij}(r)$'s were derived from the same set of configurations that were used to generate the XAFS spectra and the parameters reported in Table 5. Results include the analysis of first-shell Cu^{1+} hydration, and the Cu^{1+}/Br_n ion pair under hydrothermal conditions. [b] From the integrated $G_{CuBr}(r)$ out to 4 Å. [c] From the integrated $G_{CuO}(r)$ out to 3 Å. [d] Calculated from a modified Gaussian form fitted to the first peak in $G_{ij}(r)$ as described in ref 7.

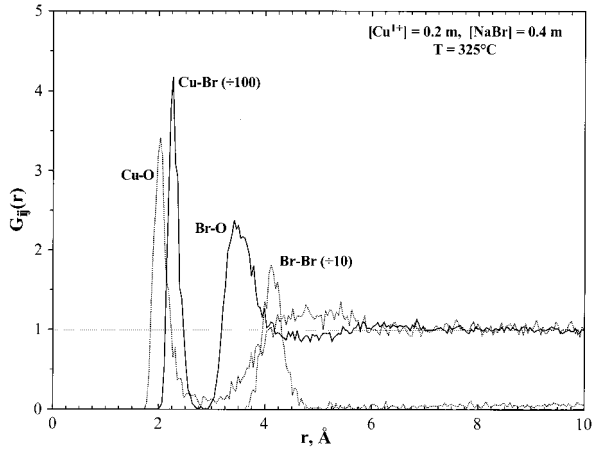

Figure 14. Pair distribution functions, $G_{ij}(r)$, from the molecular dynamics simulation for the 0.2 m Cu^{1+} and 0.4 m NaBr solution at 325 °C. The $G_{ij}(r)$'s are derived from the same set of configurations that were used to generate the EXAFS spectra in Figure 13.

supercritical conditions.[4] Unlike the $NiBr_2$ system, where the bromine ions appear to remain associated with the nickel ion almost indefinitely, one of the bromine ions eventually dissociates from the copper if the simulation is run for long times. However, it was possible to run the simulation for periods on the order of 125 ps without dissociation. Although exchange of the bromine ions between the solvent and the first solvation shell is slow, the equilibration within the first shell appears relatively rapid. Simulated XAFS spectra from different runs showed no significant differences. These spectra can be compared to the experimental spectra and used to test the degree of contact ion pairing or to test the quality of the intermolecular potentials that are used in the simulation by how well they reproduce the first shell structural details. The distances and Debye−Waller factors extracted from the MD-XAFS (Table 5) for the Cu−Br are in excellent agreement with the experimentally derived ones (Table 2) for those solutions containing excess amounts of Br^- from added NaBr.

Figure 14 presents the various radial pair distribution functions, $G_{ij}(r)$, for the $CuBr_2$/NaBr system at 325 °C. The first peak in the distribution function $G_{CuBr}(r)$ is relatively narrow and probably reflects the small size of the Cu^{1+} ion, as well as the stability of the $[CuBr_2]^-$ complex. Surprisingly, the first peak in the distribution function $G_{CuO}(r)$ is also quite narrow, which may account for the presence of the oxygen scattering in the simulated spectrum that is absent in the experimental data. One possible explanation for this extra scattering is that the simulation is over-estimating the structure of water in the first solvation shell of the copper ion resulting in a too narrow peak in the radial distribution function and a correspondingly enhanced scattering contribution from the oxygen atom on water. Another possibility is that the simulation is producing the wrong configuration of water in the first shell. Ignoring the influence of additional solvent water, a single water molecule would be expected to interact with a linear $[CuBr_2]^-$ ion in one of two configurations. The first is with the oxygen on water oriented toward the copper ion and the hydrogens facing outward, away from the complex. The second is with the hydrogens pointing toward the bromines and the oxygen pointed away from the copper. The first configuration favors the interaction between the extra electron density on the oxygen with the positive charge on the copper ion while the second configuration favors hydrogen bonding of the water protons with the negative bromine ions. Which configuration predominates in the presence of additional solvent water probably involves the cancellation of fairly large electrostatic forces. Getting the right cancellation is difficult to achieve with most models. The pair distribution function $G_{CuO}(r)$ suggests that the water orientation with the oxygen atom pointed toward the copper is dominating the simulation, but it is possible that in the experimental system it is the orientation with the hydrogens pointed at the bromine ions that predominates. The greater copper−oxygen distance for this orientation would also explain why there is no oxygen scattering in the experimental spectrum.

There are other possible reasons why the simulation fails to accurately capture the behavior of the water in the first shell about the Cu^{1+}. For instance, there may be appreciable covalent nature to the Cu−Br interaction which delocalizes the Cu charge away from the surface of the cation thus reducing the forces that drive association with water. These types of behavior might be captured by including explicit many-body terms in the potentials.

The bromine−oxygen function shows a single broad peak centered at about 3.4 Å. The broadness of this peak can be attributed to the fact that the hydrogen atoms interact strongly with the bromine ion while the oxygen atom is left to wave around freely in the solvent waters. Finally, the bromine−bromine pair distribution function shows a distinct peak centered at 4.1 Å. This is due to the two bromine ligands of the $[CuBr_2]^-$ complex. These two bromine atoms remain at a relatively fixed

distance with respect to one another, which results in a large peak in the pair distribution function. The peak is centered at twice the Cu−Br distance seen in the copper−bromine pair distribution function, which confirms that the most probable structure for the $[CuBr_2]^-$ complex in solution is a linear complex with the copper ion in the middle.

Conclusions

The structure of bromo copper(I) complexes in high-temperature water consist primarily of two-coordinated Cu species that most likely have a linear geometry. Above 200 °C, excess amounts of Br^- push the equilibrium strongly towards the linear dibromo Cu^{1+} species. Higher halide coordination species, e.g. $CuBr_3^{2-}$, were not observed, even in solutions containing 2 m NaBr. There may be significant covalent nature to the bonds of the Br^-−Cu^{1+}−Br^- species that increases its stability and decreases the interaction of the Cu^{1+} with water molecules in the first shell. Both the XANES and the EXAFS results indicate little or no water in the first coordination shell. This stands in contrast to simple potential models that predict strongly bound water in this first solvation shell. These new findings about the of Cu^{1+} behavior may lead to better thermodynamic models and will improve our understanding of the mechanisms of reactions involving Cu^{1+} species under hydrothermal conditions.

There are strong similarities in the behavior of Cu^{2+} and Ni^{2+} even though Ni^{2+} is not subject to the Jahn−Teller distortion of the axial ligand. Namely, the octahedral coordination with water persists to about 325 °C. It is also at this temperature that we start to see transitions in the coordination structure that coincides with the lowering of the dielectric constant of water suggesting that these types of coordination transitions are driven in part by electrostatic forces.

Acknowledgment. This research was supported by the Director of the Office of Energy Research, Office of Basic Energy Sciences, Chemical Sciences Division of the U.S. Department of Energy, under Contract No. DE-AC06−76RLO 1830. Work by JGD and MMH was supported by the U. S. Department of Energy, Office of Environmental Management, under Contract No. DE-AC06-76RLO 1830. Work by EAS at UW was supported by the U. S. Department of Energy, Office of Environmental Management, under Contract No. DE-FG07-97ER14818.

References and Notes

(1) Pfund, D. M.; Darab, J. G.; Fulton, J. L.; Ma, Y. *J. Phys. Chem.* **1994**, *98*, 13 102−13 107.
(2) Palmer, B. J.; Pfund, D. M.; Fulton, J. L. *J. Phys. Chem.* **1996**, *100*, 13 393−13 398.
(3) Fulton, J. L.; Pfund, D. M.; Wallen, S. L.; Newville, M.; Stern, E. A.; Ma, Y. *J. Chem. Phys.* **1996**, *105*, 2161−2166.
(4) Wallen, S. L.; Palmer, B. J.; Fulton, J. L. *J. Chem. Phys.* **1998**, *108*, 4039−4046.
(5) Seward, T. M.; Henderson, C. M. B.; Charnock, J. M.; Dobson, B. R. *Geochim. Cosmochim. Acta* **1996**, *60*, 2273−2282.
(6) Ragnarsdottir, K. V.; Oelkers, E. H.; Sherman, D. M.; Collins, C. R. *Chem. Geol.* **1998**, *151*, 29−39.
(7) Hoffmann, M. M.; Darab, J. G.; Palmer, B. J.; Fulton, J. L. *J. Phys. Chem. A* **1999**, *103*, 8471−8482.
(8) Seward, T. M.; Henderson, C. M. B.; Charnock, J. M.; Driesner, T. *Geochim. Cosmochim. Acta* **1999**, *63*, 2409−2418.
(9) Mayanovic, R. A.; Anderson, A. J.; Bassett, W. A.; Chou, I.-M. *J. Synchrotron Radiat.* **1999**, *6*, 195−197.
(10) Mountain, B. W.; Seward, T. M. *Geochim. Cosmochim. Acta* **1999**, *63*, 11−29.
(11) Xiao, Z.; Gammons, C. H.; Williams-Jones, A. E. *Geochim. Cosmochim. Acta* **1998**, *62*, 2949−2964.
(12) D′Angelo, P.; Bottari, E.; Festa, M. R.; Nolting, H.-F.; Pavel, N. V. *J. Chem. Phys.* **1997**, *107*, 2807−2812.
(13) Korshin, G. V.; Frenkel, A. I.; Stern, E. A. *Environ. Sci. Technol.* **1998**, *32*, 2699−2705.
(14) Ansell, S.; Tromp, R. H.; Neilson, G. W. *J. Phys.: Condens. Matter* **1995**, *7*, 1513−1524.
(15) Collings, M. D.; Sherman, D. M.; Ragnarsdottir, K. V. *Chemical Geology* **2000**, *167*, 65−73.
(16) Persson, I.; Sandström, M.; Steel, A. T.; Zapatero, M. J.; Åkesson, R. *Inorg. Chem.* **1991**, *30*, 4075−4081.
(17) Wallen, S. L.; Palmer, B. J.; Pfund, D. M.; Fulton, J. L.; Newville, M.; Ma, Y.; Stern, E. A. *J. Phys. Chem. A* **1997**, *101*, 9632−9640.
(18) Hoffmann, M. M.; Darab, J. G.; Heald, S. M.; Yonker, C. R.; Fulton, J. L. *Chem. Geol.* **2000**, *167*, 89−103.
(19) Ingalls, R.; Crozier, E. D.; Whitmore, J. E.; Seary, A. J.; Tranquada, J. M. *J. Appl. Phys.* **1980**, *51*, 3158−3163.
(20) Teo, B. K. *EXAFS: Basic Principles and Data Analysis*; Springer-Verlag: New York, 1986.
(21) Stern, E. A.; Heald, S. In *Handbook of Synchrotron Radiation*; Eastman, D. E., Farge, Y.; Koch, E. E., Eds.; North-Holland: Amsterdam, 1983.
(22) *X-ray Absorption: Principles, Applications, Techniques of EXAFS, SEXAFS and XANES*; Koningsberger, D. C., Prins, R., Eds.; John Wiley & Sons: New York, 1988.
(23) Stern, E. A.; Newville, M.; Ravel, B.; Yacoby, Y.; Haskel, D. *Physica B* **1995**, *208 & 209*, 117−120.
(24) Newville, M.; Livins, P.; Yacoby, Y.; Rehr, J. J.; Stern, E. A. *Phys. Rev. B* **1993**, *47*, 14126−14131.
(25) Zabinsky, S. I.; Rehr, J. J.; Ankudinov, A.; Albers, R. C.; Eller, M. J. *Phys. Rev. B* **1995**, *52*, 2995−3009.
(26) Rehr, J. J.; Mustre de Leon, J.; Zabinsky, S. I.; Albers, R. C. *J. Am. Chem. Soc.* **1991**, *113*, 5135−5140.
(27) Newville, M.; Ravel, R.; Haskel, D.; Rehr, J. J.; Stern, E. A.; Yacoby, Y. *Physica B* **1995**, *208 & 209*, 154−156.
(28) Berendsen, H. J. C.; Grigera, J. R.; Straatsma, T. P. *J. Phys. Chem.* **1987**, *91*, 6269.
(29) Dang, L. X. *The Parameters for Bromine Ion Were Supplied Personally by Liem Dang.* 1997.
(30) Dang, L. X. *J. Am. Chem. Soc.* **1995**, *117*, 6954.
(31) Kau. L.-S.; Spira-Solomon, D. J.; Penner-Hahn, J. E.; Hodgson, K. O.; Solomon, E. I. *J. Am. Chem. Soc.* **1987**, *109*, 6433−6442.
(32) Moen, A.; Nicholson, D. G.; Rønning, M. *J. Chem. Soc., Faraday Trans.* **1995**, *91*, 3189−3194.
(33) Zuo, J. M.; Kim, M.; Spence, J. C. H.; O'Keeffe, M. *Nature* **1999**, *401*, 49−52.
(34) Pickering, I. J.; George, G. N. *Inorg. Chem.* **1995**, *34*, 3142−3152.
(35) Filipponi, A.; D′Angelo, P.; Pavel, N. V.; Di Cicco, A. *Chem. Phys. Lett.* **1994**, *225*, 150−155.
(36) Minicucci, M.; Di Cicco, A. *Phys. Rev. B* **1997**, *56*, 11 456−11 464.
(37) Altorfer, F.; Graneli, B.; Fischer, P.; Bührer, W. *J. Phys.: Condens. Matter 6*, 9949−9962.
(38) Fulton, J. L.; Hoffmann, M. H.; Darab, J. G. *Chem. Phys. Lett.* **2000**, in press.